Journal of Thermal Stresses

ISSN: 0149-5739 (Print) 1521-074X (Online) Journal homepage: www.tandfonline.com/journals/uths20

An acoustic theory of thermally cracked rocks

José M. Carcione & Flavio Poletto

JOURNAL OF THERMAL STRESSES
https://doi.org/10.1080/01495739.2025.2557270

An acoustic theory of thermally cracked rocks

José M. Carcione and Flavio Poletto

Department of Geophysics, National Institute of Oceanography and Applied Geophysics - OGS, Trieste, Italy

ABSTRACT
High temperatures in rocks lead to thermal cracking, whereby porosity and permeability increase and the P and S wave velocities as well as the *Q* (quality) factor decrease. In addition, the crack density increases and the crack aspect ratio decreases. There are many ultrasonic data in the literature, usually for dry, stiff rocks (granite, basalt) and ambient pressure, which can be processed and described using appropriate theories. The data were usually measured up to a temperature of about 600–800 °C before melting of the grain minerals. In this work, we use Gassmann equations based on Pride's dry-rock moduli and estimate the consolidation coefficient, mass density, wave velocities, quality factor and permeability as a function of temperature. Fluid substitution is then applied to determine the density and velocities of the rock saturated with steam and water under supercritical conditions. The equivalent inclusion average stress (EIAS) model is used in combination with the Zener model to model attenuation and estimate crack fraction, density and aspect ratio. We compare the results with the simplified approach of O'Connell and Budiansky to determine the crack density. The permeability mainly follows power laws as a function of porosity. The inversion method uses a simulated annealing algorithm.

ARTICLE HISTORY
Received 3 July 2025
Accepted 29 August 2025

KEYWORDS
Crack aspect ratio; crack density; permeability; porosity; *Q* factor; thermal cracking; velocity

1. Introduction

High temperatures affect porosity, permeability and other rock properties such as stiffness, wave velocity and attenuation. These effects are relevant for volcanism (e.g., [1]), the extraction of geothermal energy (e.g., [2,3]), the safe design of waste repositories of any kind [4] and the monitoring of dams [5], bridges and tunnels built from granite rock.

Jones et al. [6] conducted thermal cracking experiments to investigate the role of thermal expansion in basalt and micrograniteteen. The basalt shows significant thermal cracking even when heated slowly at room pressure. Microcracking significantly increases permeability when heated above 300 °C. The authors note that this result may help to explain the narrow range of discharge temperatures around 350 °C of hydrothermal systems below sea level.

David et al. [7] investigated thermal cracking in granite and its effects on porosity, wave velocity, attenuation, electrical conductivity and permeability. They used Hudson's [8] model to determine the crack density and aspect ratio. The porosity increases almost fourfold up to 450 °C and the crack aspect ratio decreases by a factor of 2/3. The laboratory experiments were carried out at ambient pressure. In addition to acoustic measurements, crack density can also be estimated by processing optical photomicrographs of the rock. Griffiths et al. [9] applied this method to fine-grained granite samples that were damaged to varying degrees by thermal microcracking.

CONTACT José M. Carcione jcarcione@ogs.it Department of Geophysics, National Institute of Oceanography and Applied Geophysics - OGS Borgo Grotta Gigante 42/C, 34010 Sgonico, Trieste, Italy.

Darot and Reuschlé [10] reported on acoustic measurements in thermally pre-cracked granite as a function of pore and confining pressures.

Chaki et al. [11] performed laboratory experiments at ambient pressure on dry granite and observed an increase in (connected) porosity and permeability as well as a decrease in P and S wave velocities and Q factor as a function of temperature up to 600 °C. The data show significant thermal cracking above 300 °C, with a fourfold increase in porosity, a decrease in P-wave velocity from 5 to 2 km/s and a strong wave anelasticity (low quality factors).

Sun et al. [12] point out that the temperature range of 400–600 °C corresponds to the transition from brittle state to plasticity (or ductility) of granite and 400 °C may represent a critical threshold for thermal damage. The transition from brittleness to ductility plays an important role in earthquake seismology (e.g., [13,14]).

Alcock et al. [15] heated core samples at temperatures between 25 and 800 °C and measured P-wave velocity and porosity. They compared the estimated fracture density with values obtained from optical maps of microfracture damage. They conclude that the combined effects of thermal expansion and the phase transition from α to β of the quartz crystals have a pronounced effect on tensile strength (the transition occurs at 573 °C). In the case of the Earth's crust, the transition is accompanied by large changes in volume and elastic stiffness, large tensile stresses are generated by the down-temperature transition, brittle and viscous damage associated with the transition weakens the crust, and microcracking associated with the transition can facilitate fluid access to dry rock and is associated with seismicity and earthquakes [16]. In addition, Brown [17] shows that α-quartz reduces the v_P/v_S ratio, while β-quartz does not. The P-wave reflection coefficient in the α-β range increases with an increase in the modal abundance of quartz.

Our paper presents theories for modeling the stiffness, wave velocities, quality factor, permeability, crack fraction and density, and aspect ratio of thermally damaged rocks. To illustrate how the crack attributes are related, consider an oblate ellipsoid of minor and major radii r_1 and r_2, respectively. Its volume is $V_c = (4/3)\pi a r_2^3$, where $a = r_1/r_2$ is the aspect ratio. Then, the crack (soft) porosity is $\phi_c = \phi c = n_V V_c$, where c is the crack fraction, the volume fraction of the pore space composed of cracks, and n_V is the number of cracks per unit volume. Moreover, the crack density is $\epsilon = n_V r_2^3 = 3\phi c/(4\pi a) \propto c/a$ ([18], Equation 4).

The theories are mainly based on the Gassmann equations, the EIAS model (equivalent inclusion average stress), in combination with the viscoelastic Zener model, and the approach of O'Connell and Budiansky [18] and Budiansky and O'Connell [19]. We apply the theories to ultrasonic data measured in granite by David et al. [7] and Chaki et al. [11].

2. Theories

We assume that the medium is composed of solid (grains) and fluid with a porosity ϕ. The solid fraction is 1 – ϕ. The bulk density is

$$\rho = (1-\phi)\rho_s + \phi\rho_f, \tag{1}$$

where ρ_s and ρ_f are the solid and fluid densities, respectively.

Gassmann equations give the bulk and shear moduli:

$$K = \frac{K_s - K_m + \phi K_m\left(K_s/K_f - 1\right)}{1 - \phi - K_m/K_s + \phi K_s/K_f}, \tag{2}$$

and

$$\mu = \mu_m \tag{3}$$

(e.g., [20], Equation 7.35), where K_s and K_f are the solid and fluid bulk moduli, respectively, K_m and μ_m are the dry-rock bulk and shear moduli, respectively, obtained with Pride equations:

$$K_m = \frac{K_s(1-\phi)}{(1+C\phi)}, \quad \text{and} \quad \mu_m = \frac{\mu_s(1-\phi)}{(1+3C\phi/2)}, \tag{4}$$

Pride et al. [21], where C is a consolidation coefficient that represents the degree of bonding between grains. High values of C imply poor cementation or bonding, a situation expected at high temperatures.

Other theories used here are the Gassmann-consistent EIAS model in combination with Zener's viscoelastic model (see Appendices A and B), which takes attenuation into account to obtain the crack fraction, density and crack aspect ratio, and the approach of O'Connell and Budiansky [18], which provides the crack density. The EIAS model, which is based on the concept of crack fraction, differs from the second approach by modeling wave attenuation and the possibility that the cracks have a non-zero aspect ratio. The thermal crack tests are carried out at high frequencies. In the first example, we initially adopted the Gassmann equations, valid at low frequencies, as an approximation for low-loss media in order to obtain the quality factor Q. In this case, $Q \gg 1$, as shown in the following calculations, and the velocity dispersion is limited.

The seismic P and S velocities are

$$v_P = \sqrt{\frac{K + 4\mu/3}{\rho}} \quad \text{and} \quad v_S = \sqrt{\frac{\mu}{\rho}}. \tag{5}$$

To perform inversions, we minimize an objective function using a simulated-annealing algorithm developed by Goffe et al. [22], based on Corana et al. [23]. The Fortran code can be found in:

https://econwpa.ub.uni-muenchen.de/econ-wp/prog/papers/9406/9406001.txt

See Qadrouh et al. [24] for examples of application.

3. Examples

3.1. Chaki et al. [11] data

We consider the experimental velocity for granite from Chaki et al. [11, Table 2, Figures 3, 5 and 6]. Table 1 shows the data, where f_d is the dominant frequency of the spectrum, and A the relative amplitude (normalized with respect to that at $T = 105$ °C).

The following equation fits the velocity:

$$v_P(T) = v_0\left[1 + \left(1 - \frac{T^n}{T_0^n}\right) \times n \times 10^{-3}\right], \quad T_0 \le T \le T_1, \tag{6}$$

where $v_0 = 5000$ m/s at $T_0 = 105$ °C, $T_1 = 600$ °C and $n = 3.05$. Figure 1 shows the fit.

Chaki et al. [11, Table 2] provide the experimental (connected) porosity as a function of temperature. The following equation fits the data:

$$\phi = \left[\frac{100}{a_0} + \frac{(T/100)^2}{a_1} + \frac{\exp(a_2 T/100)}{2000}\right]\frac{1}{a_3}, \tag{7}$$

with T in °C, where $a_0 = 8.8$, $a_1 = 5$, $a_2 = 1.845$ and $a_3 = 16.4$. Figure 2 shows the fit.

According to Table 1 of Chaki et al. [11], the density at $T = 105$ °C is $\rho = 2687$ kg/m^3 with $\phi = 0.68\%$. The bulk density is given in equation (1). In their experiments air saturates the pore space. We assume $\rho_f = 1.208$ kg/m^3, and $K_f = 1.01 \times 10^5$ Pa. Moreover, $\rho_s = 2705$ kg/m^3. To obtain K_s and μ_s, we consider the data at $T = 105$ °C, with $\rho = 2687$ kg/m^3 and $v_P = 5000$ km/s. Then, we have a P-wave plane modulus $M = \rho v_P^2 = 67$ GPa. It is [25, Table 2.1]:

Table 1. Chaki et al. [11] Experimental data.

Temperature, T °C	Porosity, ϕ %	Velocity, v_P m/s	Frequency, f MHz	Amplitude (relative)	Permeability, κ (μ D)
105	0.68	5000	0.51	1	9.53
200	0.71	4867	0.49	0.85	10.86
300	0.81	4385	0.47	0.76	16.20
400	0.91	4067	0.45	0.58	22.87
500	1.10	3460	0.40	0.44	40.69
600	2.85	1900	0.40	0.13	733.33

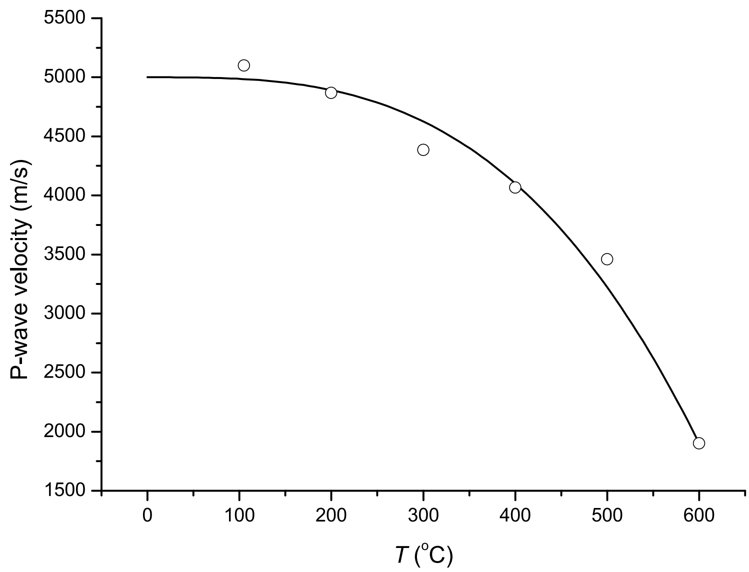

Figure 1. Fit of Chaki et al. [11] velocity as a function of temperature.

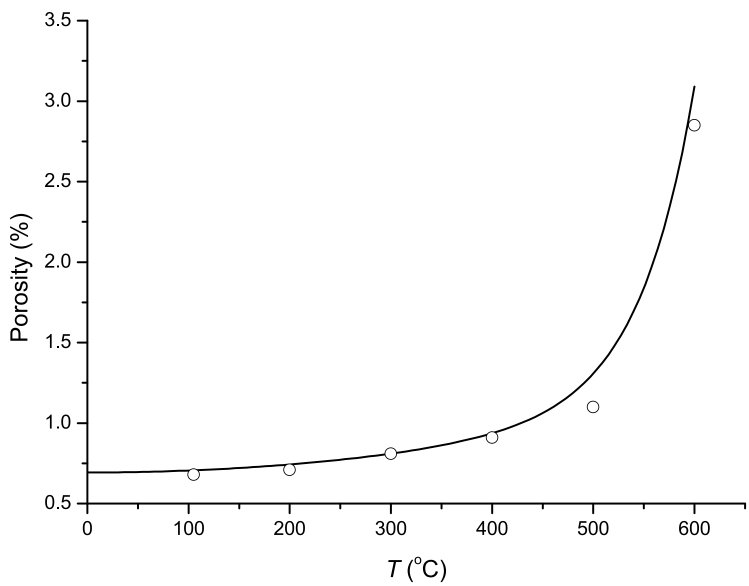

Figure 2. Fit of Chaki et al. [11] porosity as a function of temperature.

$$M = \frac{\mu(4\mu - E)}{3\mu - E}. \tag{8}$$

Then,

$$\mu = \frac{1}{8}\left(E + 3M - \sqrt{(E+3M)^2 - 16EM}\right). \tag{9}$$

However, if we consider the Young modulus proposed by Chaki et al. [11] ($E = 75$ GPa), we obtain a negative sign within the square root. Therefore their value is not realistic. We therefore assume a Young modulus $E = 58.63$ GPa, which is given in Table 6 of Schock et al. [26], which corresponds to a granite with properties similar to that of Chaki et al. [11]. We obtain $\mu = 24$ GPa and $K = M - 4\mu/3 = 35$ GPa. The values of K_s and μ_s should be greater than these values.

Next, we consider the mineralogy (see Table 2), and its moduli according to Mavko et al. [25, Table A.4.1]. The properties of mica are taken from McNeil and Grimsditcht [27, Table 1]), assuming $M = c_{33}$ and $\mu = c_{55}$. We set K_s and μ_s equal to the arithmetic average of the upper and lower Hashin-Shtrikman bounds [28] (see Appendix C). The calculation results in $K_s = 50$ GPa and $\mu_s = 30$ GPa. [The Wood, Reuss and Hill averages are 49, 55 and 52 GPa for the bulk modulus, and 27, 32 and 30 GPa for the shear modulus (see [25, Sections 4.1 and 4.5])].

In the experiments of Chaki et al. [11], thermal cracking occurs due to the α-β quartz transition. The room temperature form of quartz, α quartz, undergoes a reversible change in crystal structure to β quartz at 573 °C. This phenomenon is known as inversion and is accompanied by a linear expansion of 0.45%. This explains the large variations in mechanical and physical properties. The melting temperature of dry granite is 1215–1260 °C at ambient pressure and drops sharply in the presence of water, down to 650 °C at several hundred MPa pressure. Therefore, there is no melting in their experiments, otherwise alternative models must be employed (e.g., [29]). The values of Chaki et al. [11] (their Table 1) are $v_P = 5000$ m/s and $\phi = 0.0068$ at $T = 105$ °C, where ϕ is the connected porosity. For the inversion of the Pride consolidation coefficient C we use the simulated annealing algorithm. Figure 3 shows the fitting of the P-wave velocity and Figure 4 shows the consolidation coefficient, which indicates that the rock becomes less consolidated with increasing C at high temperatures.

The dominant frequency of the pulse spectrum (see Table 1) [11, Figure 6] can be used to obtain the quality factor of the rock. Quan and Harris [30, Equation 14] showed that for a Gaussian spectrum of variance σ^2 (bandwidth) at the source, the relationship between the quality factor Q and the dominant frequency shift Δf is as follows

$$Q = \frac{\pi\sigma^2 d}{v_P \Delta f}, \tag{10}$$

where d is the distance between source and receiver [31, Equation 10.31]. The attenuation factor is

$$\alpha = \frac{\pi f}{v_P Q} \tag{11}$$

Carcione [20, Equation 2.126].

Another method to determine the quality factor is to consider the relative amplitude of spectrum of the signal (Figure 6 in Chaki et al. [11]) and assume that the attenuation along the sample is equal to

$$A = \exp(-\alpha d), \tag{12}$$

Carcione [20, Equation 2.85], where A is the relative amplitude in Table 1. Combining this equation with [11], we obtain

Table 2. Proportion and stiffness moduli (in GPa) of the minerals.

Mineral	Proportion (%)	K	μ
plagioclase	46	75	25
quartz	42	37	44
feldspar	8	37	15
mica	4	43	13

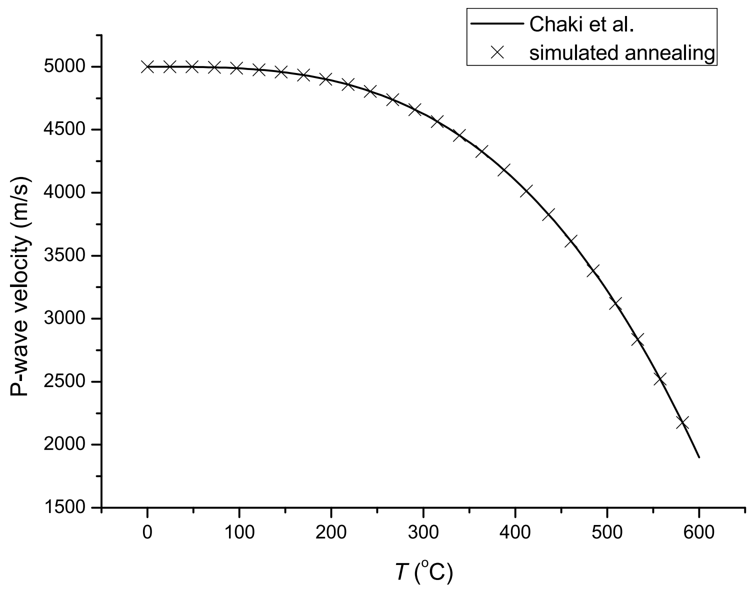

Figure 3. P-Wave velocity as a function of temperature, by using the consolidation coefficient C as a fit parameter.

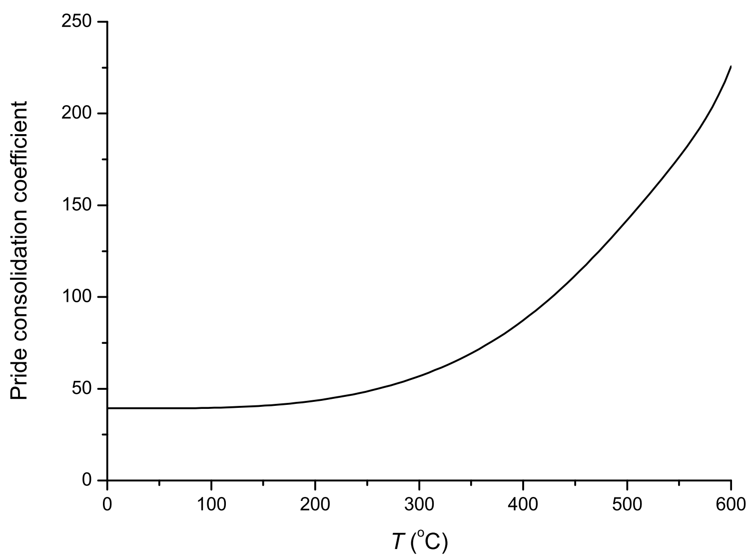

Figure 4. Consolidation coefficient C as a function of temperature. The bulk and shear moduli of the grains are $K_s = 50$ GPa and $\mu_s = 30$ GPa, respectively, constant with temperature. A high value indicates a more unconsolidated rock.

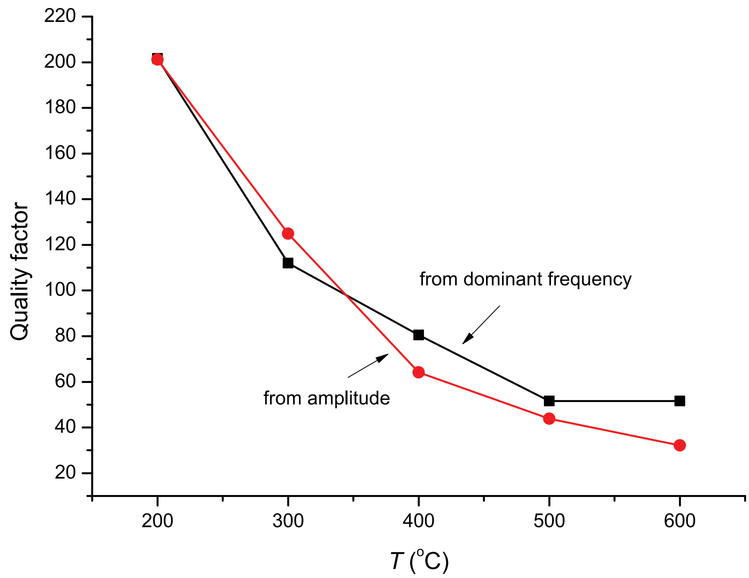

Figure 5. Quality factor as a a function of temperature obtained with two different methods.

$$Q = -\frac{\pi f d}{v_P \ln A}. \tag{13}$$

Following Quan and Harris [30, Table 1] and Figure 6 in Chaki et al. [11], $\sigma = 250\,\text{kHz}$ and $T = 105\ °\text{C}$ is assumed as the "source" spectrum, where $Q \gg 1$, and we assume $d = 10\,\text{cm}$ (e.g., [32]). Figure 5 compares the results of the two methods. Since the dominant frequency does not change from 500 to 600 °C, we have assumed that the quality factor remains constant in this interval, despite the sharp drop in velocity, which could represent a velocity dispersion with respect to temperature. As can be seen, the agreement is very good.

Next, we perform a fluid substitution by considering water in the pore space. It should be noted that the dry-rock moduli vary not only with temperature but also with the differential pressure $p_d = p_c - p$, where p_c and p are the confining and pore pressures (we have assumed an effective pressure coefficient equal to 1). In sandstones, this variation follows an exponential law as a function of p_d (e.g., [20, Equation 7.61]). In granites, it can be assumed that the dry-rock velocity follows a linear law, as shown in Figure 7 by Darot and Reuschlé [10]. The moduli then follow a quadratic law:

$$K_m = \rho_0 (v_{P0} + a p_d)^2 - \frac{4}{3}\mu_m, \qquad \mu_m = \rho_0 (v_{S0} + a p_d)^2, \qquad \rho_0 = (1 - \phi)\rho_s, \tag{14}$$

where v_{P0} and v_{S0} are the P and S velocities under atmospheric conditions measured by Chaki et al. [11] at $p_c = p = 0.1\,\text{MPa}$ and $a = 6\,\text{m/s/MPa}$ (from Darot and Reuschlé [10]), assuming that both moduli have the same value of a, taking into account that a actually corresponds to the P-wave velocity proportional to $\sqrt{K_m + 4\mu_m/3}$.

The temperature at the critical point of water is 374 °C, with a pore pressure of 22 MPa. We consider $p_c = 0.1$ (atmospheric conditions, Chaki et al. [11] data) and temperatures below the critical point. The density and wave velocity of pure water as a function of temperature and pressure are given in Appendix D.1 according to Batzle and Wang [33]. Water is a liquid at 22 MPa below the critical temperature, and at 0.1 MPa below 100 °C. Above this boiling temperature, we assume that water (in a vapor state at 0.1 MPa) has the properties of ideal gases, where

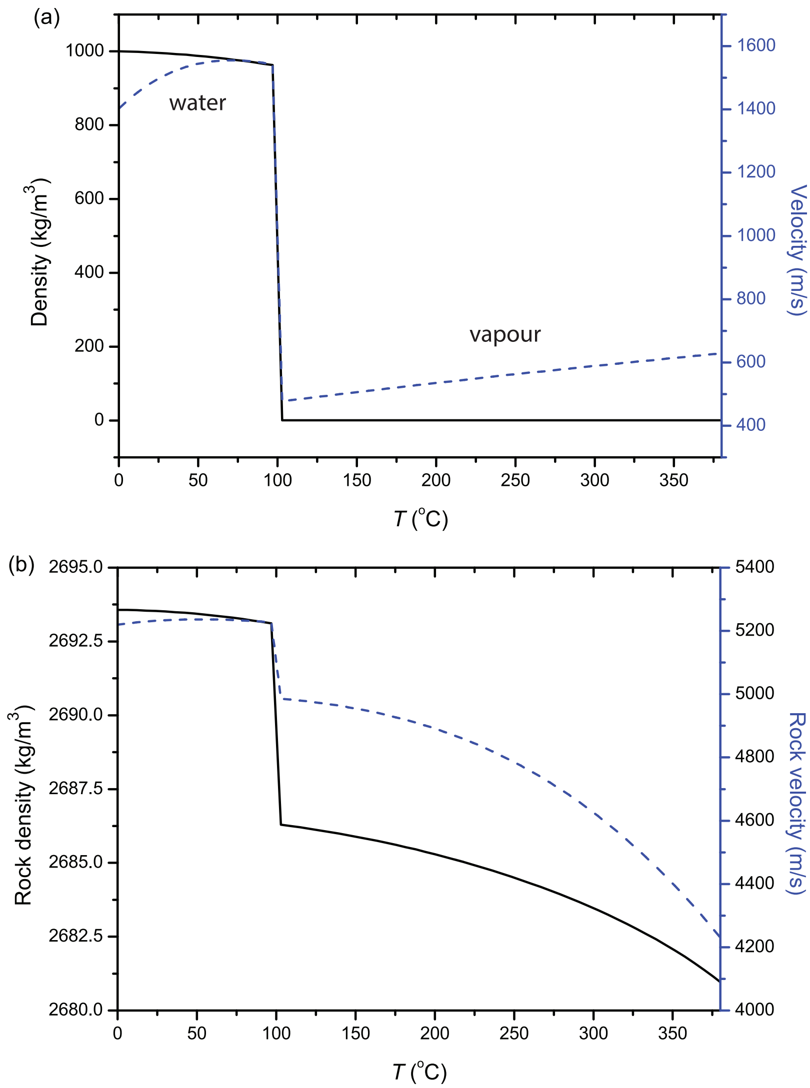

Figure 6. Density (solid line) and wave velocity (dashed line) of water-vapor (a) and saturated rock (b) as a function of temperature at atmospheric pressure (0.1 MPa). At 100 °C water becomes vapor.

$$\rho_w = \frac{pM_w}{RT}, \quad \text{and} \quad v_w = \sqrt{\frac{1.31RT}{M_w}}, \tag{15}$$

are the density and wave velocity, $R = 8.3144$ J/mol/°K, $M_w = 0.018$ kg/mol, and T is given in °K [34]. Figure 6a shows the density (a) and velocity (b) of water-vapor as a function of temperature, and Figure 6b shows the rock density and velocity.

Let us consider water at supercritical conditions (e.g., [35]), i.e., a temperature in excess of 374 °C. The Iceland Deep Drilling project involves deepening of the RN-15 well in the Reykjanes geothermal field from its original depth of 2507 m to a depth of ≈ 5 km. The well was completed on January 25, 2017 at a depth of 4659 m, where an unequilibrated bottom-hole temperature of 427 °C was recorded together with a fluid pressure of 35 MPa [36,37]. According to Suárez-Arriaga [38] the bulk modulus of water at 35 MPa and 400 °C is 0.04 GPa and the density is

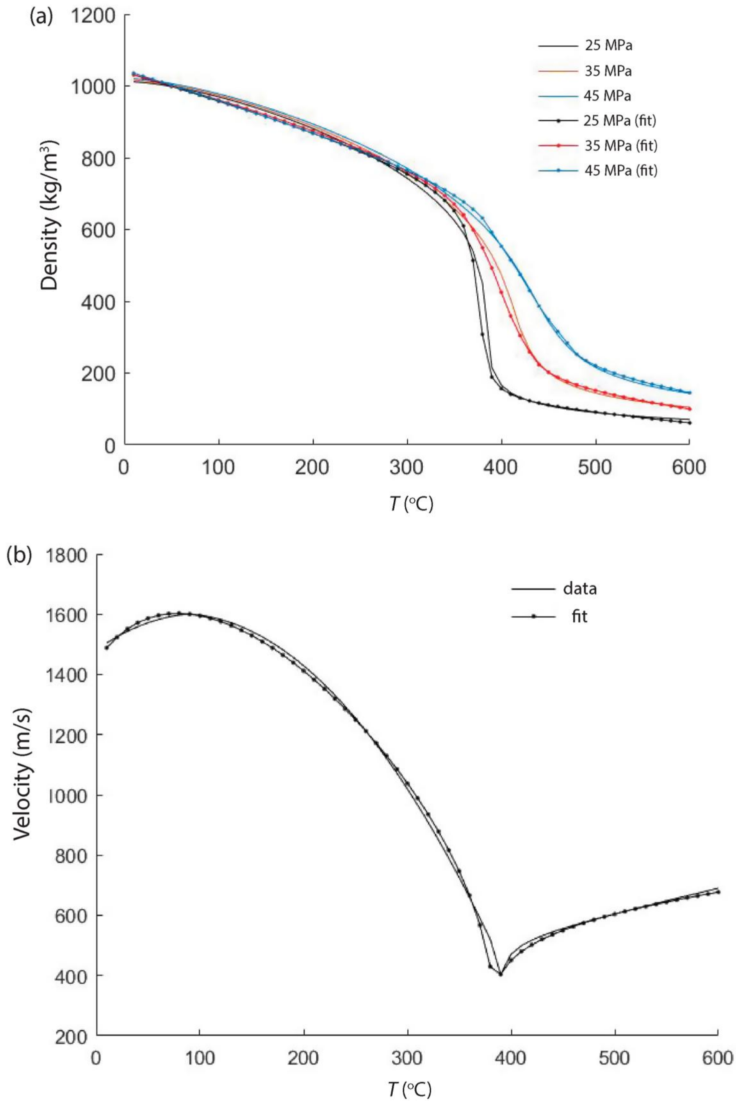

Figure 7. Approximation of the NIST data for water (see Appendix D.2). Density (a) at three different pressures, and (b) sound velocity at 25 MPa.

475 kg/m^3, with a sound velocity of 290 m/s. This results in the following P and S rock velocities: 3971 m/s and 2686 kg/m^3.

Let us now consider a pressure of 25 MPa and the entire temperature range as in Chaki et al. [11]. The density and wave velocity of pure water as a function of temperature and pressure are given in Appendix D.2 according to the National Institute of Standards and Technology (NIST) [39]. To facilitate the reproduction of the figures, we have approximated the NIST data by analytical expressions [equations (52) and (55)]. Figure 7 shows the approximation for the density and sound velocity and Figure 8 shows the bulk modulus at 25 MPa, where we have corrected outlier points in the approximations at 375.75 °C (from 711 to 311 kg/m^3), and at 387.88 °C (from 138 to 525 m/s), based on a discretization of 100 points in the temperature range. As can be seen, the bulk modulus is almost constant above the critical temperature. Figure 9a shows the density and velocity of water as a function of temperature, and Figure 9b shows the corresponding rock values.

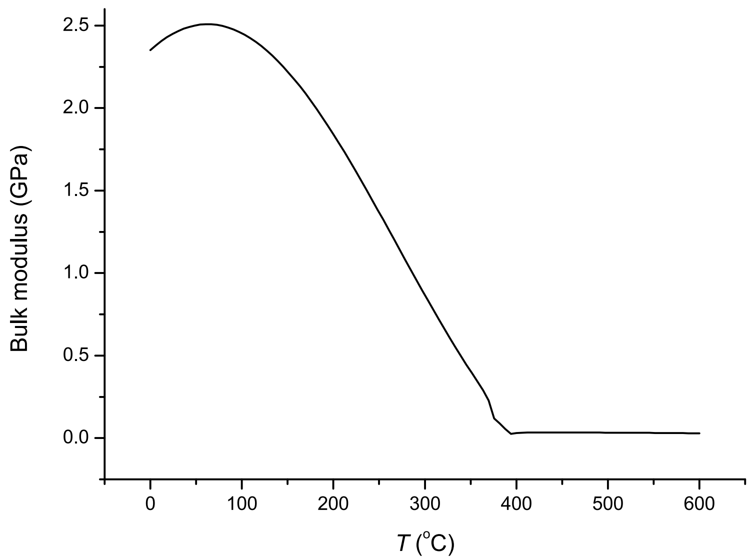

Figure 8. Bulk modulus of water as a function of temperature at 25 MPa.

In their Figure 3, Chaki et al. [11] give the relative gas permeability κ in relation to that of the intact rock, κ_0. Measurements are carried out at 20 °C and the relative pressure and the confining pressure applied to the sample are successively 0.5 and 0.8 MPa. The actual values in microdarcy (μD) are listed in Table 1, since $\kappa_0 = 9.53\ \mu$ D at $\phi_0 = 0.0068$, according to Table 1 of these authors. At very low porosity ($\phi \ll 1$), the Kozeny-Carman relationship between porosity and permeability becomes a cubic equation:

$$\kappa = \kappa_c \phi^3 \tag{16}$$

Mavko et al. [25, Section 8.4], where $\kappa_c = \kappa_0/\phi_0^3 = 3 \times 10^7\ \mu$D, obtained by calibration with the values of the intact rock (105 °C). Figure 10 shows the permeability as a function of porosity (a) and temperature (b), where the open circles represent the experimental values. We used equation (7), which relates porosity to temperature. From Tables 1, 3 and 4, we produce Figure 11, showing the permeability as a function of the crack density, (a) form the O'Connell and Budiansky [18] equations, and (b) from the EIAS model.

Based on randomly oriented and circular dry cracks, the crack density can be calculated from the velocity and mass density of the rock. The initial (intact) rock has a high-frequency P-wave velocity $v_{P0} = 5000$ m/s and a porosity of 0.68% and we assume that this initial rock has no thermal cracks. According to equation (1), the bulk density of the air-saturated rock is approximately $\rho_0 = (1-0.0068)$ 2705 kg/m3 = 2687 kg/m3. Then $M_0 = K_0 + 4\mu_0/3 = \rho_0 v_{P0}^2 =$ 67 GPa, and we have seen above that with a Young's modulus of 58.63 GPa we have $\mu_0 =$ 24 GPa and $K_0 =$ 35 GPa, where we use the sub-index "0" for the initial rock at 105°C. We consider the relationship between moduli and crack density given by O'Connell and Budiansky [18] (see [40, Section 6.7.3.2]). Since the cracks are isolated with respect to the flow, this approach simulates a very high-frequency saturated rock behaviour. O'Connell and Budiansky [18, Equations 5, 7 and 8], Schon [40, Equations 6.101–6.105] or Mavko et al. [25, Equations 4.11.1–4.11.3] give

$$K = K_0 \left[1 - \frac{16}{9}\left(\frac{1-\nu^2}{1-2\nu}\right)\epsilon\right]. \tag{17}$$

$$\mu = \mu_0 \left[1 - \frac{32}{45}\left(\frac{(1-\nu)(5-\nu)}{2-\nu}\right)\epsilon\right]. \tag{18}$$

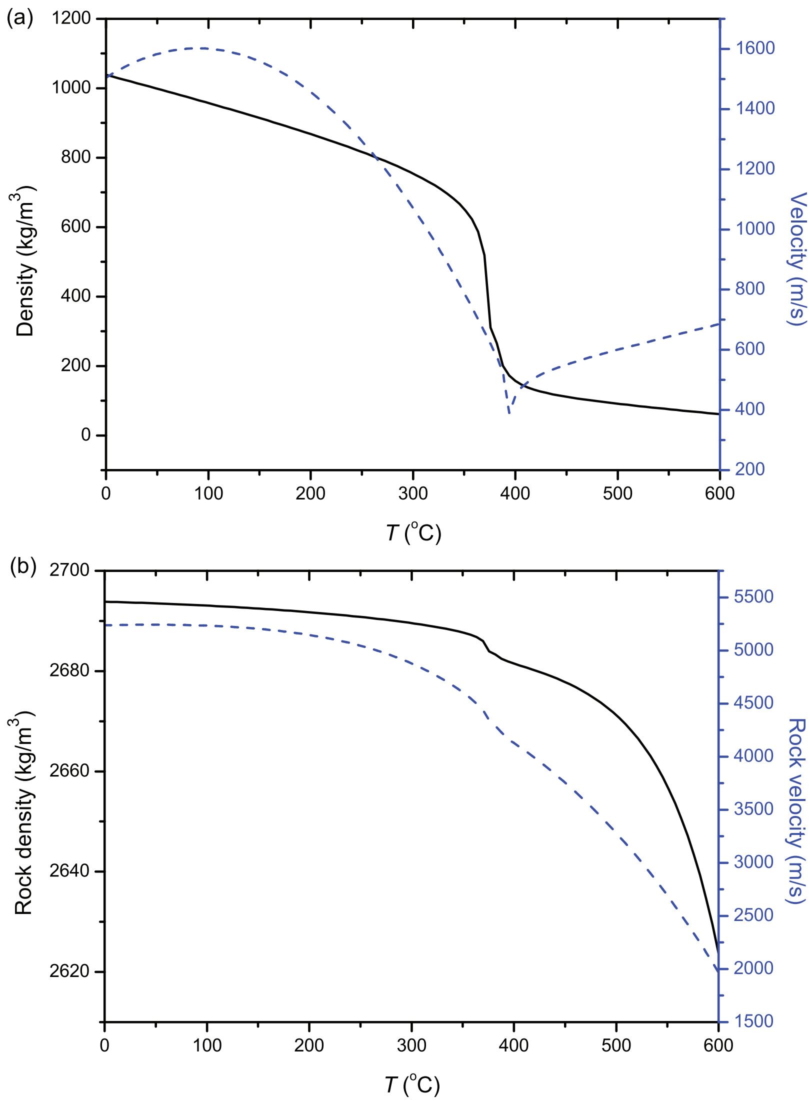

Figure 9. Density (solid line) and wave velocity (dashed line) of water (a) and saturated rock (b) as a function of temperature at 25 MPa.

with

$$\epsilon = \frac{45}{16} \frac{(\nu_0 - \nu)(2 - \nu)}{(1 - \nu^2)(10\nu_0 - 3\nu_0\nu - \nu)}, \tag{19}$$

where ν is the Poisson ratio of the cracked rock. An approximation (that we do not use in this work) is

$$\nu = \nu_0 \left(1 - \frac{16}{9}\epsilon\right), \qquad \nu_0 = \frac{3K_0 - 2\mu_0}{2(3K_0 + \mu_0)}. \tag{20}$$

If we combine equations (17) and (18), with $M_0 = \rho_0 v_{P0}^2 = K_0 + 4\mu_0/3$, we get

$$\epsilon = \frac{M_0 - M}{f(\epsilon)K_0 + \frac{4}{3}g(\epsilon)\mu_0}, \qquad f(\epsilon) = \frac{16}{9}\left(\frac{1 - \nu^2}{1 - 2\nu}\right), \qquad g(\epsilon) = \frac{32}{45}\left(\frac{(1 - \nu)(5 - \nu)}{2 - \nu}\right), \qquad \nu = \nu(\epsilon), \tag{21}$$

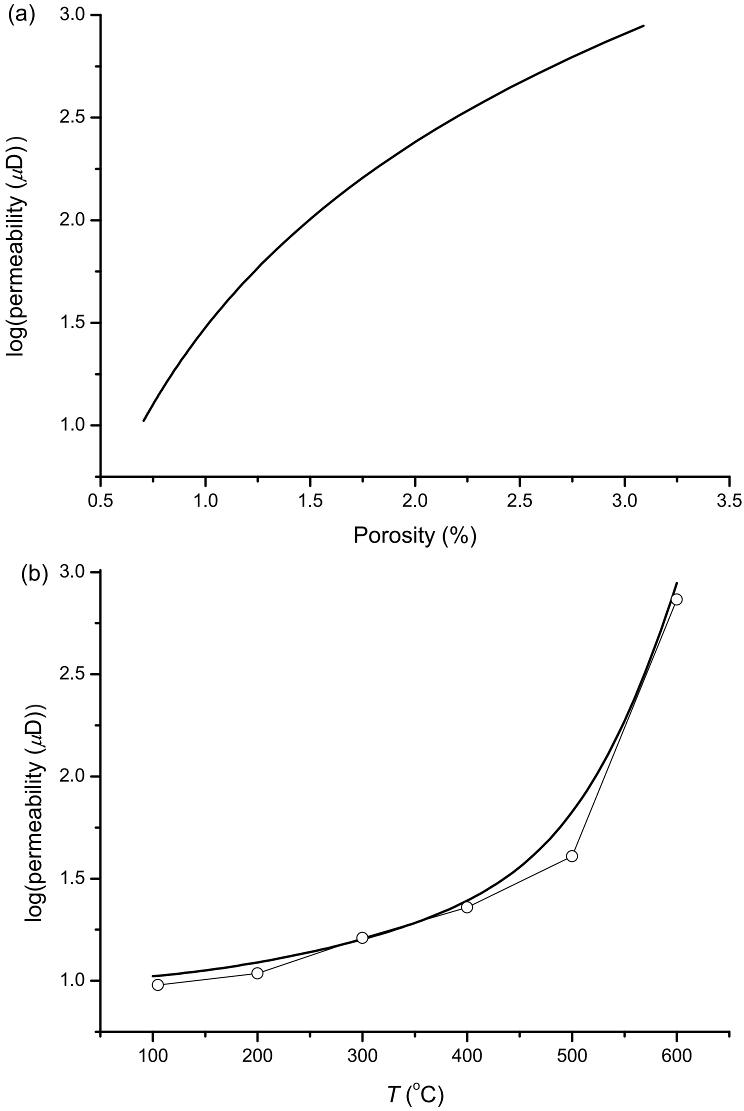

Figure 10. Permeability as a function of porosity (a) and temperature (b). The open circles are experimental values by Chaki et al. [11].

where $M = \rho v_P^2 = K + 4\mu/3$ is the P-wave modulus of the cracked rock at temperature T. We solve the nonlinear equations (19) and (21) using the simulated annealing algorithm, with ϵ and ν as unknowns, assuming initial values $\nu = \nu_0$ for each temperature (ranging from $\epsilon = 0$ at 105 °C to 0.37 at 600 °C). The crack densities, with the Poisson ratios and dry-rock moduli, are given in Table 3. We verify the simulating annealing results by solving equation (19) for ν analytically as a function of the crack density ϵ (a cubic equation), where $\nu_0 = 0.2$, $K_0 = 35$ GPa and $\mu_0 = 24$ GPa, corresponding to $T = 105$ °C. We select the root with zero imaginary part and real part between 0 and 9/16, since the moduli approach zero uniformly as ϵ increases and vanishes exactly for $\epsilon = 9/16$, as the approximation is not valid at this limit [18]. Then, we replace ν into equations (17) and (18) to obtain K and μ.

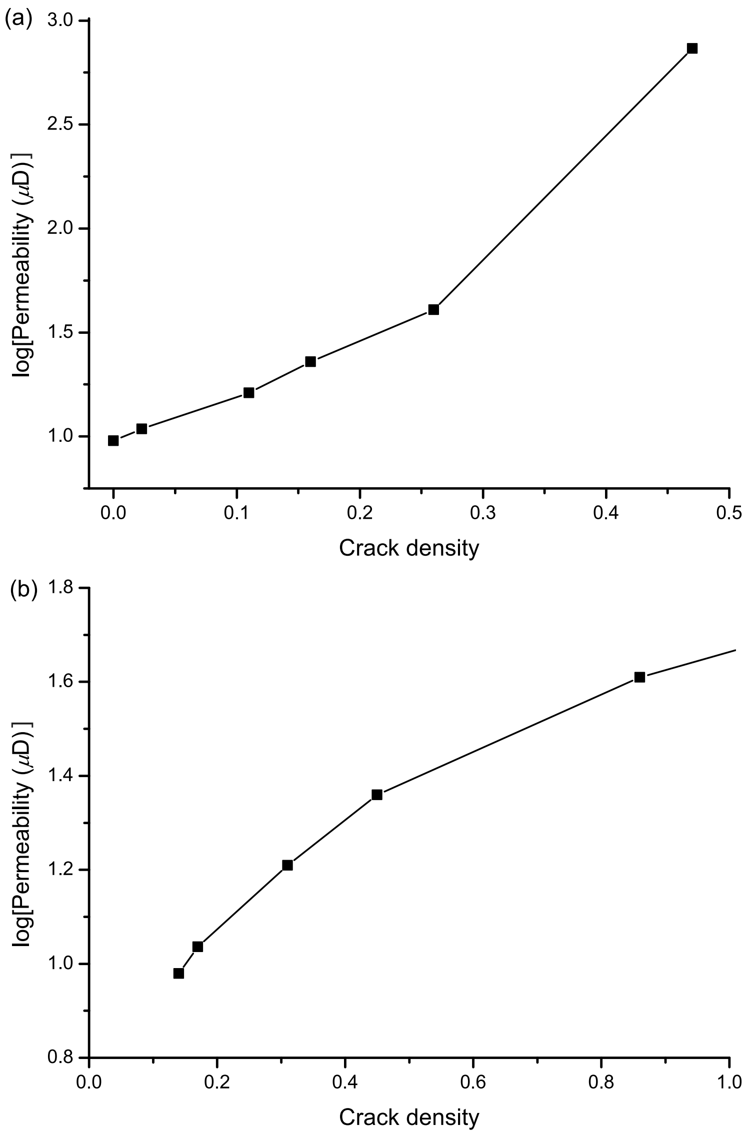

Figure 11. Permeability as a function of crack density corresponding to Chaki et al. [11] data. (a) from the O'Connell and Budiansky [18] equations; (b) from the EIAS model.

Table 3. Crack density, poisson ratio and dry-rock moduli [18] theory.

T (°C)	Crack density	ν	K (GPa)	μ (GPa)
105	0	0.20	35	24
200	0.023	0.21	33	23
300	0.11	0.18	25	20
400	0.16	0.16	21	18
500	0.26	0.12	14	14
600	0.47	0.04	3.4	4.6

Using the quality factors, we apply the EIAS-Zener model to the data to obtain the crack fraction and crack aspect ratio (see Appendices A and B and Cheng et al. [41]). We assume that water vapor is present in the pore space at ambient conditions, with $K_f = 0.13\,\text{MPa}$ and $\rho_f = 0.75\,\text{kg/m}^3$ (air, in practice).

Table 4. Properties of granite (air saturated, EIAS-zener model) [11].

T (° C)	Crack fraction	Aspect ratio	Crack density	$v_{\rm com}$ (m/s)	v_∞ (m/s)	Q_P	$v^S_{\rm com}$ (m/s)	$v^S_{\rm iso}$ (m/s)
105	1.6×10^{-2}	1.9×10^{-4}	0.14	4995	5005	500	3042	3043
200	8.9×10^{-3}	8.8×10^{-5}	0.17	4855	4979	201	2982	2085
300	1.2×10^{-2}	7.5×10^{-5}	0.31	4367	4403	124	2756	2761
400	9.4×10^{-3}	4.5×10^{-5}	0.45	4036	4099	64	2589	2597
500	4.8×10^{-3}	1.4×10^{-5}	0.86	3364	3564	44 (17)	2219	2248
600	9.0×10^{-3}	1.6×10^{-5}	4.1	1834	1973	32 (14)	1259	1284

$v_{\rm iso}$ is v_P in Table 1.

The low- and high-frequency (laboratory) P-wave velocities are (see Appendix A)

$$v_{\rm com} = \sqrt{\frac{M_{\rm com}}{\rho}}, \qquad M_{\rm com} = K_{\rm com} + 4\mu_{\rm com}/3 \tag{22}$$

and

$$v_{\rm iso} = \sqrt{\frac{M_{\rm iso}}{\rho}}, \qquad M_{\rm iso} = K_{\rm iso} + 4\mu_{\rm iso}/3 \tag{23}$$

respectively. The velocity reported in Table 1 is $v_{\rm iso}$, at 500 kHz, according to Chaki et al. [11]. We consider this value in the range $v_{\rm com} < v_{\rm iso} < v_\infty$, where $v_\infty = \sqrt{M_\infty/\rho}$, and M_∞ is the P-wave modulus [35].

The quality factor at $\omega_1 = 2\ \pi\ 500\,\text{kHz}$ can be expressed as in equation (41). The constraints in the simulated-annealing algorithm to obtain the aspect ratio and crack fraction are $a_{\rm min} = 0$, $a_{\rm max} = 1$, starting at $a = 0.5$, and $c_{\rm min} = 10^{-8}$, $c_{\rm max} = 1$, starting at $c = 10^{-5}$.

The crack porosity is $c\phi$, the part of the pore space occupied by cracks, while the rest is occupied by stiff (uniform) spherical pores. The crack density is defined as

$$\epsilon = \frac{3\phi c}{4\pi a} \tag{24}$$

Gurevich [42, eq. 36], Schon [40, Equation 6.108], Adelinet et al. [43, eq. 5]; Sun et al. [44, Equation 10], and Carcione [20, eq. 7.609]. As can be seen, the crack fraction can be in principle determined from equation (24) as $c = 4\pi\epsilon a/(3\phi)$, but the crack aspect ratio a is required, a property not considered in the theory of O'Connell and Budiansky [18].

Table 4 shows the results, with the velocities in the 5th and 6th columns corresponding to the P-wave and those in the last two columns to the S-wave. As Sun et al. [44] and Cheng et al. [41, Figure 2] show, the EIAS and CPEM (Cracks and Pores Effective Medium) models provide similar results, whereby the uncertainty in the estimation of the crack density and aspect ratio is around 15%, as Sun et al. [45] report. We consider the quality factors of Figure 5 based on the amplitude and the algorithm recalculates them (in parentheses). The crack fraction behaves in a wavelike manner depending on the temperature. There is no monotonic relationship between the crack fraction and the quality factor Q_P, but an increasing crack density and a decreasing aspect ratio correlate with a higher attenuation (lower Q_P). As shown in Figure 1 of Endres and Knight [46], Figure 2 in Cheng et al. [41] and Figure 7.22 in Carcione [20], the bulk modulus dispersion and thus the bulk attenuation does not behave monotonically as a function of the crack fraction. The quality factor Q_P of the P-wave depends on the crack fraction c *via* the dispersion index [44, Equation 46].

$$D = \frac{v_\infty}{v_{\rm com}} - 1 \approx 1/Q_P, \qquad v_\infty = x\sqrt{\frac{M_{\rm com}}{\rho}} = x\ v_{\rm com}, \tag{25}$$

Table 5. Properties of La Peyratte granite (air saturated) [7].

Rock	ϕ (%)	Crack density	Aspect ratio	Crack fraction	$v_P = v_{\rm iso}$ (m/s)	Q_P
intact	0.35	0.075 (0.078)	0.0130 (3.3 $\times$ 10^{-5})	(3.1 $\times$ 10^{-3})	5450	140
220 °C	0.57	0.139 (0.230)	0.0098 (1.1 $\times$ 10^{-5})	(1.9 $\times$ 10^{-3})	4836	23
450 °C	0.87	0.245 (0.740)	0.0085 (1.2 $\times$ 10^{-5})	(4.5 $\times$ 10^{-3})	3729	25 (16)

The values in parentheses are our calculations with the EIAS model.

Table 6. Properties of La Peyratte granite (water saturated, EIAS-Zener model).

Rock	$v_0 = v_{\rm com}$ (m/s)	$v_P = v_{\rm iso}$ (m/s)	Q_P	Permeability (μD)
intact	5701	5832	21	0.006
220 °C	5409	5671	10	0.678
450 °C	4916	5344	5	1.570

The permeability is data from Table 2 of David et al. [7].

(see Appendix A.1), such that

$$Q_P \approx \frac{1}{x-1}, \tag{26}$$

an approximation of equation (41). At constant aspect ratio a, the dissipation factor Q_P^{-1} has a maximum at intermediate values of c (see Figure 7.22 in Carcione [20]) with zero values (no attenuation) at $c=0$ and 1, while the shear dispersion increases from zero to a maximum at $c=1$. For the same value of Q_P, we can have two different crack fractions. If a single pore shape is present ($c=0$ or 1), the incremental fluid pressure is the same in all pores, so that no P-wave dispersion occurs at these limits. For mixed pore shapes, the induced fluid pressure change is greater in the cracks than in the spherical pores, and dispersion occurs. Table 4 also shows that the aspect ratio decreases with temperature and the crack density increases with values higher than those in Table 3, which result from the theory of O'Connell and Budiansky [18], which assumes zero aspect ratio and no attenuation. Attenuation increases with crack density [44]. Abnormal behavior occurs at 600 °C with a crack density greater than 1. There is a significant drop in P-wave velocity from 500 °C (3460 m/s) to 600 °C (1900 m/s). Between 500 and 600 °C, the samples are severely damaged due to the anisotropic expansion associated with the α/β quartz transition that occurs at 573 °C and room pressure.

A Q_S quality factor could be defined as in equation (25), where v_∞ is replaced by $v_{\rm iso}$, but it is not representative of the true factor, since we need v_∞ and this can only be determined by measurements, which allows the calculation of shear relaxation times.

3.2. Example 2: David et al. [7] data

David et al. [7] report on the properties of two samples of La Peyratte granite at 220 and 450 °C. The samples were heated at a low rate (18 °C per minute) until the maximum temperature was reached. The temperature is then kept constant for one hour. Then the system is cooled down at the same low rate to avoid temperature shocks during the heating/cooling cycle.

La Peyratte granite consists of 40% plagioclase, 2.6% K-feldspar, 24% quartz and 10% biotite [47]. Based on this composition, the effective bulk and shear modulus of the grains, calculated with a Voigt-Reuss-Hill average, David et al. [7] obtain $K_s = 52$ GPa and $\mu_s = 31.2$ GPa, respectively, and the composite density is $\rho_s = 2660$ kg/m^3. According to David et al. [7], the intact and thermally cracked rocks have the crack density and aspect ratio reported in their Table 3, obtained from the elastic moduli of the grains and P-wave velocity and density. They do not use the measured quality factors to obtain these values. From the data of David et al. [7] in their Table 3 we obtain $c = 4\pi\epsilon a/(3\phi) = 1.170$, 1.001 and 1.002 for the intact rock, the 220 °C sample

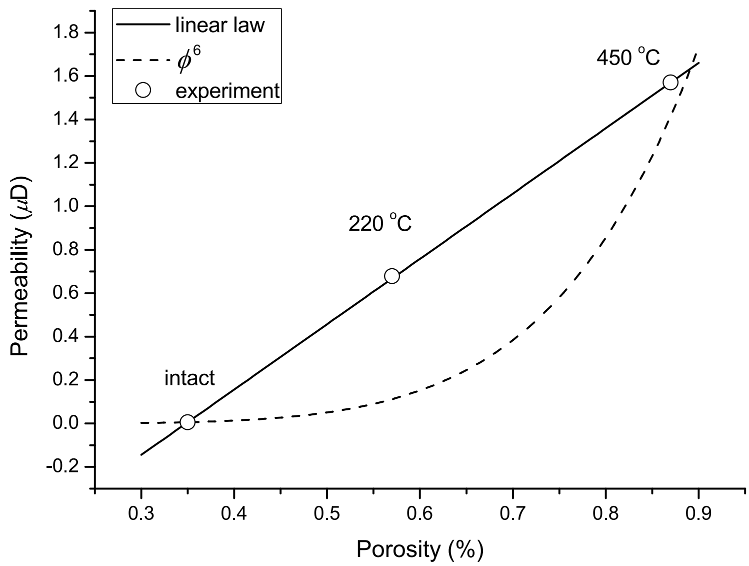

Figure 12. Permeability as a function of porosity. The open circles are experimental values by David et al. [7].

and the 450 °C sample, respectively. However, c cannot be greater than 1. We report their values in Table 5 in addition to the values for porosity, P-wave velocity and quality factors.

We invert for the crack density and aspect ratio with the simulated annealing algorithm to fit the velocities and quality factors, using the crack fraction c and aspect ratio a as fit parameters. We use the EIAS theory in combination with the Zener attenuation model to obtain the low- and high-frequency P-wave velocities (and moduli) and quality factors. The value of c must be between 0 and 1 and cannot assume these two limits because the EIAS model does not predict attenuation at these limits. As above, we assume that water vapor is present in the pore space at ambient conditions. The velocity reported in Table 5 is $v_{\rm iso}$, at 700 kHz, according to David et al. [7]. The quality factor at $\omega_1 = 2\ \pi\ 700\,\text{kHz}$ can be expressed as in equation (41). The values for ϵ and a that fit the data are given in parentheses in Table 5. We obtained a value of 16 for the quality factor of the 450 °C sample, in contrast to the value of 25 obtained by David et al. [7]. However, the quality factor should decrease with increasing crack density (compared to 23 for the 220 °C sample) as predicted by our calculations. The experimental negative correlation between attenuation and induced thermal damage is attributed by David et al. [7] to the fact that the 450 °C sample is the only one with a length significantly different from that of the reference sample. If we replace steam or air by water ($K_f = 2.22\,\text{GPa}$, $\rho = 1000\,\text{kg/m}^3$), we obtain the velocities and quality factors listed in Table 6.

The permeability in David et al. [7] has been measured at an effective pressure of 3 MPa on the water saturated samples. Table 6 lists the permeability, which follows an almost linear law as a function of porosity, as can be seen in Figure 12, where the open circles represent the data and the solid line represent the function

$$\kappa = A\phi + B, \qquad A = 300.7\ \mu\text{D}, \qquad B = -1.046\ \mu\text{D}. \tag{27}$$

The dashed line corresponds to a power law,

$$\kappa = \kappa_c \phi^6, \tag{28}$$

where $\kappa_c = 3.26 \times 10^{12}\ \mu$D. Both behaviors are anomalous and deviate significantly from the Kozeny-Carman laws. The experiments to obtain permeability in David et al. [7] show some contradictions, such as a reversal of the trend in permeability with increasing damage (see their Table 2, last row).

Next, the velocities are determined from the crack densities, calculated with the EIAS model, using the equations of O'Connell and Budiansky [18] in order to compare the two theories. The initial (intact) rock has a high-frequency P-wave velocity $v_P = 5450$ m/s, and a porosity of 0.35%. According to equation (1), the bulk density of the air saturated rock is approximately $\rho_0 = (1-0.0035)$ 2660 kg/m3 = 2651 kg/m3. Then $M_0 = \rho_0 v_{P0}^2 =$ 79 GPa. David et al. [7] report mineral Lamé constants $\lambda_s =$ 31.3 GPa and $\mu_s =$ 31.2 GPa. Then $K_s = \lambda_s + 2\mu_s/3 =$ 52 GPa and $M_s = \lambda_s + 2\mu_s =$ 93.5 GPa. Using Pride equations (4), we have

$$M = \rho v_P^2 = K_m + \frac{4}{3}\mu_m = (1-\phi)\left[\frac{K_s}{(1+C\phi)} + \frac{4}{3}\frac{\mu_s}{(1+3C\phi/2)}\right], \tag{29}$$

which gives a quadratic equation in C:

$$\begin{aligned} &AC^2 + BC + C = 0, \\ &A = \frac{3\phi^2 M}{2(1-\phi)}, \\ &B = \phi\left[\frac{5M}{2(1-\phi)} - \frac{3K_s}{2} - \frac{4\mu_s}{3}\right], \\ &C = \frac{M}{1-\phi} - M_s \end{aligned} \tag{30}$$

Solving the equation gives consolidation coefficients $C = 43$, 73 and 147 for the intact rock, 220 °C and 450 °C, respectively. Using the crack densities computed with the EIAS-Zener model, give the P-wave velocities (equation (5)) 5295, 4404 m/s and an imaginary value, respectively, indicating that the two theories are not fully compatible. The solutions corresponding to the exact solution of the problem with ϵ and ν as unknowns, i.e., with an objective function based on equations (19) and (21) gives $\epsilon = 0$, 0.09 and 0.25 [with $K(\mu)$: 45(25), 33(22), 17(15) GPa] for the intact rock, 220 °C and 450 °C, respectively. The values of ϵ are closer to the results of David et al. [7] in Table 5, as expected, since they used a similar model [8], that is consistent with that of O'Connell and Budiansky [18].

3.3. Additional data

Jones et al. [6] report on crack density (Figure 4, values from 0 to 0.05) and permeability (Figure 5) in basalt as a function of temperature. Crack density is calculated from ultrasonic velocities (not given) using the method of O'Connell and Budiansky [18]. The permeability ranges from 1 to 10 nanodarcy. Oven-dried rock samples were heated at ambient pressure at a rate of 1 °C/min to various peak temperatures up to 800 °C. A low heating rate was used to ensure that cracking was due to temperature alone and not to thermal gradients in the sample. Samples were heated to their peak temperature, held for 1 h and then cooled to room temperature at 1 °C/min. Due to lack of data (mineral properties, density, velocity and attenuation) analysis is not possible

Griffiths et al. [9, Table 2] provide data on the porosity and P-wave velocity of Garibaldi gray granite samples as a function of temperature, measured at room temperature and pressure. The heating procedure consisted of drying the rock in a vacuum pump at 40 °C for 24 h before placing the sample in the oven, which was programmed to heat at 1 °C/min to the desired maximum temperature. The rock remained at the target temperature for two hours before being heated again at a temperature of 1 °C/min before being cooled back down to room temperature. Due to the lack of data (mineral properties, density and attenuation), analysis is not possible.

Recently, Alcock et al. [15] reported new data on thermally treated core samples from Devon granite. The samples were thermally treated at temperatures between 25 and 800 °C. Their Table 1 shows the mineralogy, and their Table 2 the density, P-wave velocity and porosity as a function of temperature. The mass density ranges from 2.62 to 2.52 g/cm^3, the porosity from 1 to 8% and the velocity from 4.7 to 0.5 km/s. The crack density is obtained from optical images, and the P-wave velocity is calculated from the crack density according to the method of O'Connell and Budiansky [18]. However, there is a significant discrepancy between the experimental (their Table 2) and numerical (their Table 5) values, with a difference of 1.85 km/s at 800 °C.

The discrepancies in crack density between the EIAS and O'Connell-Budiansky models are due to the different physical foundations of the two theories. In contrast to the work of Budiansky and O'Connell [19], the EIAS model describes the pore structure as a continuous spectrum of pore shapes instead of dividing the pore space into two categories: spherical pores and very thin cracks. Furthermore, the EIAS model allows the cracks to have a non-zero aspect ratio, and the theory of Budiansky and O'Connell [19] uses a self-consistent formulation; therefore, their result is not compatible with the Gassmann-Biot theory,

4. Conclusions

We consider experiments published in the literature on the acoustics of thermally cracked (stiff) rocks (granite, basalt) and propose appropriate models to describe the data. The results show that the proposed models can explain the experiments. These concern dry rocks at ambient pressure, where the dry-rock moduli play the main role. The Hashin-Shtrikmann bounds and the Voigt-Reuss-Hill mean are used to obtain the mineral properties, and the Gassmann equations, based on a consolidation coefficient calculated with a simulated annealing method, are used to fit the P-wave velocity as a function of temperature. In addition, the quality factor, which decreases with temperature, is determined using two different methods, namely from the amplitude decay and from the dominant frequency of the signal spectrum. Both results agree very well. Subsequently, a fluid substitution is performed in which the rock is saturated with water at ambient and supercritical conditions. The acoustic properties of water are based on the NIST data and we propose explicit expressions for the density and bulk modulus. We obtain the crack fraction, crack density and aspect ratio from the wave velocity using two different approaches, namely the EIAS-Zener model and the equations of O'Connell and Budiansky. The first model can be used to predict the attenuation of the saturated rock. As expected, the quality factor decreases with temperature and decreasing aspect ratio, and the density increases with temperature. The permeability is satisfactorily described by a power law relationship to porosity with powers of 3 and 6, although in the latter case only two permeability values are given. The proposed equations and methods can be useful for monitoring acoustic properties in various applications such as volcanism, geothermal energy and nuclear waste disposal sites.

Disclosure statement

No potential conflict of interest was reported by the author(s).

Data availability statement

The data are available from the corresponding author on request.

References

[1] S. Vinciguerra, C. Trovato, P. G. Meredith and P. M. Benson, "Relating seismic velocities, thermal cracking and permeability in Mt. Etna and Iceland basalts," *Int. J. Rock Mech. Min. Sci.*, vol. 42, no. 7-8, pp. 900–910, 2005. DOI: 10.1016/j.ijrmms.2005.05.022.

[2] B. Farina, F. Poletto, D. Mendrinos, J. M. Carcione and C. Karytsas, "Seismic properties in conductive and convective hot and super-hot geothermal systems," *Geothermics*, vol. 82, pp. 16–33, 2019. DOI: 10.1016/j.geothermics.2019.05.005.

[3] G. G. Meyer, G. Shahin, B. Cordonnier and M. Violay, “Permeability partitioning through the brittle-to-ductile transition and its implications for supercritical geothermal reservoirs,” *Nat. Commun.*, vol. 15, no. 1, 2024, pp. 1–9. DOI: 10.1038/s41467-024-52092-0.
[4] L. Wang, Y. Wu, Z. Huang, J. Lin, Y. Wang and W. Zhang, “Effects of temperature and confining pressure on the permeability of Beishan granite from high-level radioactive waste disposal repository,” *Case Stud. Therm. Eng.*, vol. 55, pp. 104111, 2024. DOI: 10.1016/j.csite.2024.104111.
[5] J. Enzell, R. Malm and M. Tollsten, “Predicting the influence of seasonal thermally induced cracking on a reinforced concrete arch dam,” *KSCE J. Civil Eng.*, vol. 26, no. 6, pp. 2707–2721, 2022. DOI: 10.1007/s12205-022-0112-7.
[6] C. Jones, G. Keaney, P. G. Meredith and S. A. F. Murrell, “Acoustic emission and fluid permeability measurements on thermally cracked rocks,” *Phys. Chem. Earth*, vol. 22, no. 1-2, pp. 13–17, 1997. DOI: 10.1016/S0079-1946(97)00071-2.
[7] C. David, B. Menéndez and M. Darot, “Influence of stress-induced and thermal cracking on physical properties and microstructure of La Peyratte granite,” *Int. J. Rock Mech. Min. Sci.*, vol. 36, no. 4, pp. 433–448, 1999. DOI: 10.1016/S0148-9062(99)00010-8.
[8] J. A. Hudson, “Wave speeds and attenuation of elastic waves in material containing cracks,” *Geophys. J. R. Astr. Soc.*, vol. 64, no. 1, pp. 133–150, 1981. DOI: 10.1111/j.1365-246X.1981.tb02662.x.
[9] L. Griffiths, M. J. Heap, P. Baud and J. Schmittbuhl, “Quantification of microcrack characteristics and implications for stiffness and strength of granite,” *Int. J. Rock Mech. Min. Sci.*, vol. 100, pp. 138–150, 2017. DOI: 10.1016/j.ijrmms.2017.10.013.
[10] M. Darot and T. Reuschlé, “Acoustic wave velocity and permeability evolution during pressure cycles on a thermally cracked granite,” *Int. J. Rock Mech. Min. Sci.*, vol. 37, no. 7, pp. 1019–1026, 2000. DOI: 10.1016/S1365-1609(00)00034-4.
[11] S. Chaki, M. Takarli and W. P. Agbodjan, “Influence of thermal damage on physical properties of a granite rock: porosity, permeability and ultrasonic wave evolutions,” *Constr. Build. Mater.*, vol. 22, no. 7, pp. 1456–1461, 2008. DOI: 10.1016/j.conbuildmat.2007.04.002.
[12] Q. Sun, W. Zhang, L. Xue, Z. Zhang and T. Su, “Thermal damage pattern and thresholds of granite,” *Environ. Earth Sci.*, vol. 74, no. 3, pp. 2341–2349, 2015. DOI: 10.1007/s12665-015-4234-9.
[13] J. M. Carcione and F. Poletto, “Seismic rheological model and reflection coefficients of the brittle-ductile transition,” *Pure Appl. Geophys.*, vol. 170, no. 12, pp. 2021–2035, 2013. DOI: 10.1007/s00024-013-0643-4.
[14] W. A. Elders, G. O. Friðleifsson and A. Albertsson, “Drilling into magma and the implications of the Iceland Deep Drilling Project (IDDP) for high-temperature geothermal systems worldwide,” *Geothermics*, vol. 49, pp. 111–118, 2014. DOI: 10.1016/j.geothermics.2013.05.001.
[15] T. Alcock, D. Bullen, P. M. Benson and S. Vinciguerra, “Temperature-driven micro-fracturing in granite: the interplay between microstructure, mineralogy and tensile strength,” *Heliyon*, vol. 9, no. 3, pp. e13871, 2023. DOI: 10.1016/j.heliyon.2023.e13871.
[16] S. E. Johnson, W. J. Song, A. C. Cook, S. S. Vel and C. C. Gerbi, “The quartz α-β phase transition: does it drive damage and reaction in continental crust?,” *Earth Planet. Sci. Lett.*, vol. 553, pp. 116622, 2021. DOI: 10.1016/j.epsl.2020.116622.
[17] D. Brown, “The α-β quartz transition in some common continental crust rocks: implications for Crustal Seismology,” *Terra Nova*, vol. 37, no. 4, pp. 209–215, 2025. DOI: 10.1111/ter.12768.
[18] R. J. O’Connell and B. Budiansky, “Seismic velocities in dry and saturated solids,” *J. Geophys. Res.*, vol. 79, no. 35, pp. 5412–5426, 1974., DOI: 10.1029/JB079i035p05412.
[19] B. Budiansky and R. J. O’Connell, 1980, “Bulk dissipation in heterogeneous media,” in *Solid Earth Geophysics and Geotechnology*, S. Nemat-Nasser, Ed. New York: The American Society of Mechanical Engineers, pp. 1–10.
[20] J. M. Carcione, 2022, *Wave Fields in Real Media. Theory and Numerical Simulation of Wave Propagation in Anisotropic, Anelastic, Porous and Electromagnetic Media*, 4th ed. Amsterdam: Elsevier.
[21] S. R. Pride, J. G. Berryman and J. M. Harris, “Seismic attenuation due to wave-induced flow,” *J. Geophys. Res.*, vol. 109, pp. B01201.1–B01201.19, 2004.
[22] W. L. Goffe, G. D. Ferrier and J. Rogers, “Global optimization of statistical functions with simulated annealing,” *J. Econom.*, vol. 60, no. 1–2, pp. 65–99, 1994. DOI: 10.1016/0304-4076(94)90038-8.
[23] A. Corana, M. Marchesi, C. Martini and S. Ridella, “Minimizing multimodal functions of continuous variables with the simulated annealing algorithm,” *ACM Trans. Math. Softw.*, vol. 13, no. 3, pp. 262–280, 1987. DOI: 10.1145/29380.29864.
[24] A. N. Qadrouh, J. M. Carcione, M. Alajmi and M. M. Alyousif, “A tutorial on machine learning with geophysical applications,” *Boll. Geof. Teor. Appl.*, vol. 60, pp. 375–402, 2019.
[25] G. Mavko, T. Mukerji and J. Dvorkin, 2020, *The Rock Physics Handbook: Tools for Seismic Analysis in Porous Media*. Cambridge: Cambridge University Press.
[26] R. N. Schock, A. E. Abey, H. C. Heard and H. Louis, *Mechanical Properties of Granite from the Taourirt Tan Afella Massif*, Algeria: UCRL-51296, Lawrence Livermore Laboratory, 1972.

[27] L. E. McNeil and M. Grimsditcht, “Elastic moduli of muscovite mica,” *J. Phys. Condens. Matter*, vol. 5, no. 11, pp. 1681–1690, 1993. DOI: 10.1088/0953-8984/5/11/008.

[28] Z. Hashin and S. Shtrikman, “A variational approach to the theory of the elastic behaviour of multiphase materials,” *J. Mech. Phys. Solids*, vol. 11, no. 2, pp. 127–140, 1963. DOI: 10.1016/0022-5096(63)90060-7.

[29] J. M. Carcione, B. Farina, F. Poletto, A. N. Qadrouh and W. Cheng, “Seismic attenuation in partially molten rocks,” *Phys. Earth Planet. Inter.*, vol. 309, pp. 106568, 2020. DOI: 10.1016/j.pepi.2020.106568.

[30] Y. Quan and J. M. Harris, “Seismic attenuation tomography using the frequency shift method,” *Geophysics*, vol. 62, no. 3, pp. 895–905, 1997. DOI: 10.1190/1.1444197.

[31] V. Saxena, M. Krief and L. Adam, *Handbook of Borehole Acoustics and Rock Physics for Reservoir Characterization*. Amsterdam: Elsevier, 2018.

[32] F. Homand-Etienne and R. Houpert, “Thermally induced microcracking in granites: characterization and analysis,” *Int. J. Rock Mech. Min. Sci. Geomech. Abst*, vol. 26, no. 2, pp. 125–134, 1989. DOI: 10.1016/0148-9062(89)90001-6.

[33] M. Batzle and Z. Wang, “Seismic properties of pore fluids,” *Geophysics*, vol. 57, no. 11, pp. 1396–1408, 1992. DOI: 10.1190/1.1443207.

[34] S. W. Kieffer, “Sound speed in liquid-gas mixtures: water-air and water-steam,” *J. Geophys. Res.*, vol. 82, no. 20, pp. 2895–2904, 1977. DOI: 10.1029/JB082i020p02895.

[35] T. Reinsch, *et al.*, “Utilizing supercritical geothermal systems: a review of past ventures and ongoing research activities,” *Geotherm Energy*, vol. 5, no. 1, pp. 16, 2017. DOI: 10.1186/s40517-017-0075-y.

[36] G. O. Fridleifsson and W. A. Elders, “The Iceland Deep Drilling project: a search for deep unconventional geothermal resources,” *Geothermics*, vol. 34, no. 3, pp. 269–285, 2005., DOI: 10.1016/j.geothermics.2004.11.004.

[37] G. Ó. Friðleifsson, *et al.*, “The Iceland Deep Drilling Project at Reykjanes: drilling into the root zone of a black smoker analog,” *J. Volcanol. Geotherm. Res.*, vol. 391, pp. 106435, 2020. DOI: 10.1016/j.jvolgeores.2018.08.013.

[38] M. C. Suárez-Arriaga, “Thermodynamics of deep supercritical geothermal systems,” *IOP Conf. Ser. Earth Environ. Sci.*, vol. 249, pp. 012019, 2019. DOI: 10.1088/1755-1315/249/1/012019.

[39] M. W. Chase, Jr., “NIST-JANAF Themochemical Tables, Fourth Edition,” *J. Phys. Chem. Ref. Data, Monogr.*, vol. 9, pp. 1–1951, 1998.

[40] J. H. Schon, 2011, *Physical Properties of Rocks: A Workbook.* Amsterdam: Elsevier.

[41] W. Cheng, J. M. Carcione, A. Qadrouh, M. Alajmi and J. Ba, “Rock anelasticity, pore geometry and the Biot-Gardner effect,” *Rock Mech. Rock Eng.*, vol. 53, no. 9, pp. 3969–3981, 2020. DOI: 10.1007/s00603-020-02155-7.

[42] B. Gurevich, “Elastic properties of saturated porous rocks with aligned fractures,” *J. Appl. Geophys*, vol. 54, no. 3–4, pp. 203–218, 2003. DOI: 10.1016/j.jappgeo.2002.11.002.

[43] M. Adelinet, J. Fortin and Y. Guéguen, “Dispersion of elastic moduli in a porous-cracked rock: theoretical predictions for squirt flow,” *Tectonophysics*, vol. 503, no. 1–2, pp. 173–181, 2011. DOI: 10.1016/j.tecto.2010.10.012.

[44] Y. Sun, J. M. Carcione and B. Gurevich, “Squirt-flow seismic dispersion models: A comparison,” *Geophys. J. Int.*, vol. 222, no. 3, pp. 2068–2082, 2020b. DOI: 10.1093/gji/ggaa274.

[45] C. Sun, J. V. M. Borgomano, J. Fortin and S. Wang, “Effect of pore collapse and grain crushing on the frequency dependence of elastic wave velocities in a porous sandstone,” *Rock Mech. Rock Eng.*, vol. 53, no. 11, pp. 5081–5093, 2020a. DOI: 10.1007/s00603-020-02213-0.

[46] A. Endres and R. Knight, “Incorporating pore geometry and fluid pressure communication into modeling the elastic behavior of porous rock,” *Geophysics*, vol. 62, no. 1, pp. 106–117, 1997. DOI: 10.1190/1.1444110.

[47] M. P. Turpault, “*Etude des mécanismes des altérations hydrothermales dans les granites fissures*,” PhD thesis, Université de Poitiers, 1989.

[48] J. G. Berryman, “Long-wavelength propagation in composite elastic media II. Ellipsoidal inclusions,” *J. Acoust. Soc. Am*, vol. 68, no. 6, pp. 1820–1831, 1980. DOI: 10.1121/1.385172.

[49] J. G. Berryman, “Mixture theories for rock properties. Rock Physics and Phase Relations. A Handbook of Physical Constants,” *AGU Ref. Shelf*, vol. 3, pp. 205–228, 1995.

Appendix A. EIAS model

The soft or crack porosity is very sensitive to the effective pressure and has a great influence on the stiffness of the rock, in contrast to the equant or stiff porosity, which occupies almost the entire pore space. The EIAS model (Equivalent Inclusion Average Stress) is used to determine the wave velocities and the quality factor as a function of the crack aspect ratio [46]. The EIAS model is based on an effective medium theory with pores and cracks of oblate spheroidal shape. The model assumes that the stiff pores are spheres and the soft pores are spheroidal (penny-shaped) cracks with an aspect ratio a, and that the cracks are hydraulically isolated from the pores at high frequencies. If the pore space is filled with a fluid of volume modulus K_f, the corresponding high frequency moduli are

$$K_{\rm iso} = K_s + \frac{\phi(K_f - K_s)\gamma}{1 - \phi(1-\gamma)}, \qquad \mu_{\rm iso} = \frac{\mu_s(1-\phi)}{1-\phi(1-\delta)}, \tag{31}$$

$$\gamma = (1-c)P_1 + cP_2, \qquad \delta = (1-c)Q_1 + cQ_2, \tag{32}$$

where c is the crack fraction [46, Equations 32, 33, 54 and 55]; [20, Section 7.22],

$$\begin{aligned}
P_1 &= \frac{K_s + 4\mu_s/3}{K_f + 4\mu_s/3},\\
P_2 &= \frac{K_s}{K_f + \pi a\beta}, \qquad \beta = \mu_s \cdot \frac{3K_s + \mu_s}{3K_s + 4\mu_s},\\
Q_1 &= 1 + \mu_s/\xi, \qquad \xi = \frac{\mu_s}{6}\cdot\frac{9K_s + 8\mu_s}{K_s + 2\mu_s},\\
Q_2 &= \frac{1}{5}\left[1 + \frac{8\mu_s}{\pi a(\mu_s + 2\beta)} + 2\cdot\frac{K_f + 2\mu_s/3}{K_f + \pi a\beta}\right],
\end{aligned} \tag{33}$$

where P_1 and Q_1 correspond to spherical pores and P_2 and Q_2 are approximations for penny-shaped cracks [25,48,49, p. 247].

The effective moduli, when complete fluid pressure communication occurs (low frequencies), are

$$\begin{aligned}
K_{\rm com} &= K_s + \frac{\phi K_s(K_f - K_s)\gamma_0}{(1-\phi)(K_s - K_f) + \left[K_f + \phi(K_s - K_f)\right]\gamma_0},\\
\mu_{\rm com} &= \frac{\mu_s(1-\phi)}{1-\phi(1-\delta_0)}.
\end{aligned} \tag{34}$$

Endres and Knight [46, Equations 34 and 35], Sun et al. [44], and Carcione [20, Section 7.22], where

$$\gamma_0 = (1-c)P_{01} + cP_{02}, \qquad \delta_0 = (1-c)Q_{01} + cQ_{02}, \tag{35}$$

$$\begin{aligned}
P_{01} &= P_1(K_f = 0) = 1 + \frac{3K_s}{4\mu_s}, \qquad P_{02} = P_2(K_f = 0) = \frac{K_s}{\pi a\beta},\\
Q_{01} &= Q_1(K_f = 0) = Q_1, \qquad Q_{02} = Q_2(K_f = 0) = \frac{1}{5}\left[1 + \frac{4\mu_s}{\pi a}\cdot\frac{\mu_s + 8\beta}{3\beta(\mu_s + 2\beta)}\right].
\end{aligned} \tag{36}$$

The moduli $K_{\rm com}$ and $\mu_{\rm com}$ with $K_f = 0$, are the dry-rock moduli to be used in Gassmann equations, i.e.,

$$K_m = \frac{K_s(1-\phi)}{1+\phi(\gamma_0 - 1)}, \qquad \mu_m = \frac{\mu_s(1-\phi)}{1+\phi(\delta_0 - 1)}, \tag{37}$$

since those moduli with $K_f \neq 0$ [Equations (34)] are identical to the Gassmann moduli (Eqs. (52) and (53) in Endres and Knight [46]). Expressions [38] are similar to equations (4). Values of a and c can be obtained by fitting the relaxed and unrelaxed moduli.

Appendix B. EIAS-Zener attenuation model.

We model the wave attenuation with the Zener element, whose P-wave complex modulus is

$$M(\omega) = M_0\left(\frac{1+\mathrm{i}\omega\tau_\epsilon}{1+\mathrm{i}\omega\tau_\sigma}\right) \tag{38}$$

Carcione [20, Section 2.4.3], where τ_ϵ, τ_σ are P-wave relaxation times, the relaxed modulus M_0 is obtained for $\omega = 0$, and the unrelaxed modulus

$$M_\infty = M_0\left(\frac{\tau_\epsilon}{\tau_\sigma}\right), \qquad (M_0 \leq M_\infty) \tag{39}$$

for $\omega \to \infty$.

We set $M_0 = M_{\mathrm{com}} = K_{\mathrm{com}} + 4\mu_{\mathrm{com}}/3$, according to the EIAS model, and $M_{\mathrm{iso}} = K_{\mathrm{iso}} + 4\mu_{\mathrm{iso}}/3$ is the modulus at the working frequency in the laboratory, say ω_1. We locate the Zener relaxation peak at

$$\omega_1 = \frac{1}{\tau}, \qquad \tau = \sqrt{\tau_\epsilon\tau_\sigma}. \tag{40}$$

At this frequency the quality factor has the minimum value

$$Q = \frac{2\tau}{\tau_\epsilon - \tau_\sigma} = \frac{2}{x - 1/x}, \qquad x = \sqrt{\frac{\tau_\epsilon}{\tau_\sigma}}. \tag{41}$$

Then, for $Q \gg 1$,

$$M_{\mathrm{iso}} \approx M_0 \mathrm{Re}\left(\frac{1+\mathrm{i}\omega_1\tau_\epsilon}{1+\mathrm{i}\omega_1\tau_\sigma}\right) = M_0 \mathrm{Re}\left(\frac{1+\mathrm{i}x}{1+\mathrm{i}/x}\right) = \frac{2M_0}{1+1/x^2}, \tag{42}$$

where we have used equations (39) and (40). Solving for x,

$$x = \left(\frac{2M_{\mathrm{com}}}{M_{\mathrm{iso}}} - 1\right)^{-1/2}, \tag{43}$$

which can be replaced in equation (41) to obtain the quality factor.

Appendix C. grain stiffness moduli.

Defining the solid proportions by p_i, for n minerals, the following relation holds

$$\sum_{i=1}^{n} p_i = 1. \tag{44}$$

The Hashin-Shtrikman upper (+) and lower (–) bounds for the bulk and shear moduli are

$$\begin{aligned} K^{\mathrm{HS}\pm} &= \Lambda(\mu_\pm), \\ \mu^{\mathrm{HS}\pm} &= \Gamma[\xi(K_\pm, \mu_\pm)], \end{aligned} \tag{45}$$

where

$$\Lambda(\mu_\pm) = \left\langle \frac{1}{K + \frac{4}{3}\mu_\pm} \right\rangle^{-1} - \frac{4}{3}\mu_\pm, \tag{46}$$

$$\Gamma(\xi) = \left\langle \frac{1}{\mu + \xi} \right\rangle^{-1} - \xi, \tag{47}$$

$$\xi(K_\pm, \mu_\pm) = \frac{\mu_\pm}{6} \left(\frac{9K_\pm + 8\mu_\pm}{K_\pm + 2\mu_\pm} \right) \tag{48}$$

(e.g., [25]), and the subscripts + and – denote the maximum and minimum moduli of the single constituents. The brackets $\langle \cdot \rangle$ indicate an average over the constituents weighted by their volume fractions. The density is simply the arithmetic average of the densities of the single constituents weighted by the corresponding volume fractions.

Appendix D. Density and bulk modulus of water.

D.1. Batzle and Wang equations

The properties of water depend on temperature and pressure. The equations are restricted to the pressures and temperatures of the experiments performed by Batzle and Wang [33] (about 60 MPa and 100 °C).

The density of water in g/cm^3 is

$$\rho_w = 1 + 10^{-6}(-80T - 3.3T^2 + 0.00175T^3 + 489p - 2Tp + 0.016T^2p - 1.3 \times 10^{-5}T^3p - 0.333p^2 - 0.002Tp^2), \tag{49}$$

where T is given in °C and p in MPa.

The sound velocity is

$$v_w = \sum_{i=0}^{4} \sum_{j=0}^{3} w_{ij} T^i p^j, \tag{50}$$

with constants w_{ij} given in Table 1 of Batzle and Wang [3].

Finally, the bulk modulus is

$$K_w = \rho_w v_w^2. \tag{51}$$

D.2. NIST equations

The National Institute of Standards and Technology (NIST) provides data about the properties of water at a wide range of temperatures and pressures [13]. The temperature at the critical point of water is 374 °C, with a pore pressure of 22 MPa.

Our analytical expression for the density is

$$\rho_w(T, p) = AH(T_0) + B[1 - H(T_0)], \tag{52}$$

where

$$A = \frac{1000}{T_0^{a_1}} - a_2 T_0 + a_3, \tag{53}$$

Table 7. Coefficients to fit the NIST density.

Pressure (MPa)	a_1	a_2	a_3	a_4	a_5	a_6
25	0.9	0.25	110	0.085	0.65	600
35	0.6	0.30	118	0.200	0.60	900
45	0.5	0.30	120	0.400	0.75	1190

$$B = 2000 - [1 - H(T_0)]\left[\frac{1000}{(-T_0)^{a_4}} + a_5 T_0 + a_6\right]. \tag{54}$$

$H(T)$ is the Heaviside function, $T_0 = T - T_h$, where T_h is 374, 400 and 430 °C for 25, 35 and 45 MPa, respectively, and Table 7 gives the coefficients a_i.

On the other hand, we consider the velocity or sound speed at 25 MPa, whose analytical expression is

$$v_w = \begin{cases} V(x = 90 - T), & 0 \le T < 90^{\circ}\mathrm{C} \\ V(x = T - 90), & 90 \le T < 385^{\circ}\mathrm{C} \\ -\dfrac{1000}{(T - 385)^{b_1}} + b_2(T - 385) + b_3, & T \ge 385\ ^{\circ}\mathrm{C} \end{cases} \tag{55}$$

where

$$V(x) = 1602\left[1 - (50x)^2 D^{-1}\right], \tag{56}$$

$D = 3.33 \times 10^8$, $b_1 = 0.9$, $b_2 = 0.8$ and $b_3 = 522$. The bulk modulus is given in equation (51).